Hindawi
Mathematical Problems in Engineering
Volume 2024, Article ID 6183332, 15 pages
https://doi.org/10.1155/2024/6183332

Research Article

ADRC and IFOC Control of a Sensorless Induction Motor Driven by a Multilevel Converter Using SVM Approach and PV Generators

Abdellah Oukassi,[1] **Oumaymah Elamri**,[2] **and Zakaria Boulghasoul**[1]

[1]*Systems and Applications Engineering Laboratory (LISA), National School of Applied Sciences (ENSA), University Cadi Ayyad University, Marrakesh, Morocco*
[2]*LAMIGEP, Emsi of Marrakech, Marrakesh, Morocco*

Correspondence should be addressed to Oumaymah Elamri; oumaymahelamri@gmail.com

Received 28 August 2023; Revised 13 March 2024; Accepted 21 March 2024; Published 15 April 2024

Academic Editor: Dhanamjayulu C

This paper offers a system for an electric vehicle. It consists of digitally controlling an induction motor without using a speed sensor. The machine is powered by a five-level cascading H-bridge inverter. The SVM control principle is used to manage the status of the five-level inverter; this removes harmonics. The H-bridge inverter converter is powered by photovoltaic sources via a serial converter, using the maximum power point tracker control principle. This structure can also reduce shading losses. In the absence of a mechanical sensor, a dynamic model of the asynchronous machine is utilized with the state variables defined in the stator reference frame. The state vector consists of the components of the rotor flux and stator current. The article provides a comparison of two methods widely used on an induction motor drive. The adaptive model-reference system method and Luenberger observer are evaluated using an active control strategy to reject disturbances to minimize the impact of disturbances. The operating principles of each method are described, and the mathematical models of training systems are developed. Both methods provide a promise for high-speed estimate applications in simulation environments. The simulation results obtained show the correct operation of both observers. Perfect decoupling between the velocity and flow control loops is observed, taking into account any disturbances that may affect the system.

1. Introduction

Induction motors are widely used in a variety of industrial applications, particularly in flexible speed systems, as a result of their robustness, high performance, reliability, and cost-effectiveness [1]. However, the main challenge of induction motors lies in the need for a more complex control system and the nonlinear coupling between torque and flux. To solve this problem, several speed control techniques have been developed for induction motors. Among these, indirect vector control, or indirect-field-oriented control (IFOC), is the most commonly used because of its efficiency [2].

However, indirect vector control is associated with certain challenges, such as high torque ripple, which is influenced by the harmonic distortion in the current. It is essential to note that the harmonic distortion in the current primarily stems from the characteristics of the inverter used in the system. In this context, the choice of inverter plays a crucial role in reducing current harmonics [3].

Renewable energy, as the name suggests, is an energy source that is permanently available for use. In recent years, interest in the use of renewable energies has increased to reduce reliance on fossil fuels for the production of electrical energy, particularly with photovoltaics [4].

It is well known that the use of photovoltaic panels is a major challenge, as it is not linear. The energy recovered from photovoltaic modules depends on the climatic conditions. Each module has the best operating point, known as the maximum power point (MPP), which is heavily influenced by lighting intensity. To recover maximum power from PV modules, it is necessary to adapt the photovoltaic panels to load. This adjustment is done by using a boost

converter, which controls maximum power with an algorithm based on the perturbation and observation method (P&O) [5, 6]. To give maximum power from the photovoltaic generator, the inverter is used. The output voltage and frequency of the inverter can be adjusted. In many applications, control of inverter output voltage is often required. Therefore, each PV module was linked to a DC/DC converter, and the modular structure was chosen [7].

Multilevel inverters (MLIs) have recently attracted growing interest in the supply of vector-controlled induction motors due to their many advantages over conventional two-level inverters and the increasing improvement in system performance [8]. Among the various MLI topologies, five-level inverters (FLIs) are particularly well known for their ability to generate five output voltage levels [9]. In this way, they produce a quasi-sinusoidal output voltage with a better harmonic spectrum. In the literature, several FLI topologies have been proposed, including the flying-capacitor topology and the cascaded H-bridge clamped at the neutral point (HBCI) [10]. Of these multilevel structures, the HBCI has the greatest potential and is used in a variety of applications. It is distinguished by its modular structure. FL-HBCI based on vector control offers a better response in terms of speed and phase current and improves performance in terms of torque ripple [11].

Proportional-integral (PI) controllers are classical controllers widely used in various industrial applications, especially in the induction motor driving industry, because of their easy implementation and simple structure. However, the use of PI controllers presents several limitations in terms of control system performance. It is highly sensitive to noise from disturbance and may lead to significant losses in efficiency due to its shallow regulation. In addition, in cases of disturbance, a long recovery time is required [12]. To overcome these limitations, researchers have developed a robust control system called the active disturbance rejection controller (ADRC). This controller was first suggested in 1998 by Han [13] and has since been further developed by many other researchers [3, 14]. ADRC allows you to reduce output noise and solve problems arising from parameter uncertainty and problems. The ADRC can be used in the following areas: automated steering control for maintaining vehicle track [15] and controlling the position of hydraulic actuators [16]. Furthermore, it significantly improves the system's robustness to external disturbances and parameter variations. In this regard, PI controllers can be replaced with ADRC controllers in a useful way.

Nowadays, researchers are paying more and more attention to sensorless speed controls [17, 18]. One of the main reasons is that using a speed sensor can be costly while making control systems more reliable, durable, robust, and affordable. Indeed, these systems can operate efficiently in the face of variations in machine resistances. However, to be able to estimate and know the motor speed, it is necessary to have a suitable estimator. In this context, several techniques are commonly used to restore the speed position. These include the adaptive model reference system (MRAS), the fuzzy sliding mode observer, the extended Kalman filter, and the Luenberger observer (LO) [19–21]. This paper investigates the behavior of two methods, MRAS and Luenberger observers, with inductive motors controlled by indirect vector control.

The major contribution of this article is the proposal of a robust sensorless vector control system for an induction motor powered by a five-level cascaded H-bridge using PV sources. The switches of this converter are handled by an algorithm based on the SVM approach. The reference voltages used at the input of the SVM control are based on the use of three active interference rejection controllers (mechanical speed, stator direct current, and stator quadratic current). This proposal is based on the use of three ADRCs. Two estimation methods, namely the Luenberger observer and MRAS, are used to estimate the motor speed. The main objective is to achieve high robustness, optimum accuracy, and response speed. A comparative analysis is carried out between the two selected estimators applied to FL-HBCI. MATLAB-Simulink simulation results are used to verify the performance of proposed systems, assess their reliability, and test their effectiveness under different conditions.

This paper is organized as follows: Section 2 presents the mathematical model of the complete system block diagram. Section 3 presents the ADRC controller. Section 4 illustrates the adaptive scheme for the MRAS estimator and the Luenberger estimator. Section 5 reports the simulation results, and Section 6 presents the conclusions.

2. The System Description

The proposed ADRC-IFOC diagram for the FL-HCBI induction motor powered without a sensor is shown in Figure 1. The system is composed of several interconnected subsystems. In the power supply section, photovoltaic generators feed the MLI via a boost converter. The output voltages of the MLI are applied directly to the induction machine. A Luenberger observer or MRAS is used to reproduce the mechanical speed variable in the absence of a sensor. Using this device, speed can be compared with a reference using a control law based on the ADRC approach. Adding the indirect method IFOC to this approach, the system generates the signals required to drive the SVM control vectors.

2.1. Photovoltaic Sources Controlled by MPPT. In this application, the photovoltaic array used to power the multilevel converter comprises three panels. A modular structure has, therefore, been chosen, with each photovoltaic module linked to a DC/DC converter. The photovoltaic generator model is shown in Table 1 [22].

The I_{pv} is a photo-generated current (A), current provides information on the spectrum of the photovoltaic cell. In practice, its evolution is linked to ambient temperature and irradiation G. Its formula is as follows:

$$I_{pv} = \frac{G}{G_r}\left(I_{scr} - k_i(T - T_r)\right). \tag{1}$$

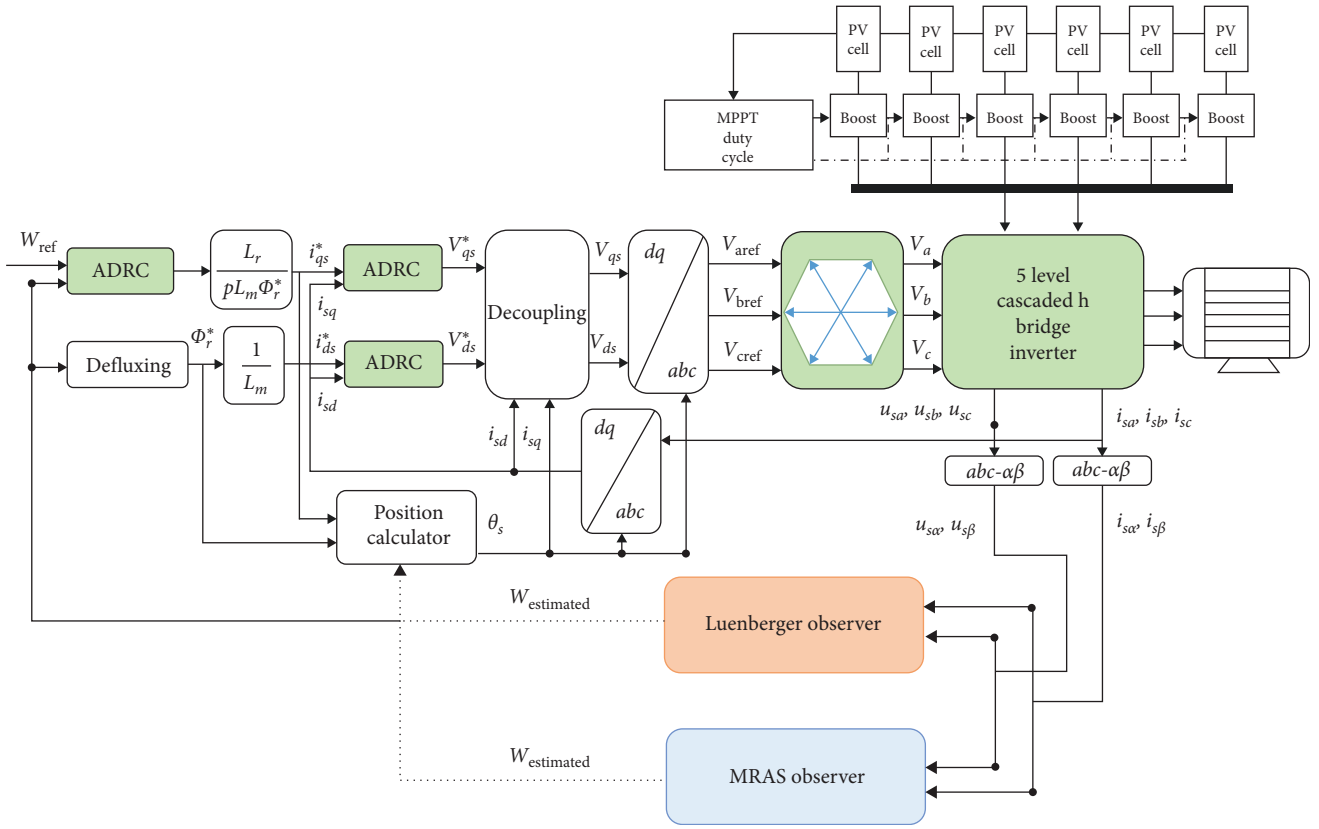

FIGURE 1: Block diagram of the proposed system.

TABLE 1: PV device specifications (1 kW/m^2, 25°C).

Symbol	Parameter	Value
K	Boltzmann constant	1.38065e–23 J/K
I_{scn}	Nominal SC current	8.21 A
V_{ocn}	Nominal OC voltage	32.9 V
K_v	Temperature voltage constant	0.123 K
K_i	Temperature current constant	0.003 K
N_s	Number of series connected cells	48
R_s	Series resistor	0.221 Ω
R_{sh}	Shunt resistor	415.405 Ω
T	Nominal temperature	298 K

T_r is the reference temperature, I_{scr} is the cell's short circuit current at T_r, k_i is the temperature coefficient of the short-circuit, and G_r is the nominal irradiation. The diode saturation current I_0 depending on temperature is expressed by the following:

$$I_0 = I_{0r}\left(\frac{T}{T_r}\right)^3 e^{\left(\frac{qE_g}{Ak}\left(\frac{1}{T_r}-\frac{1}{T}\right)\right)}, \quad (2)$$

where I_{0r} is the nominal saturation current and E_g is the band gap energy.

The current–voltage relationship of the photovoltaic panels is a complex and nonlinear function (Figure 2). The

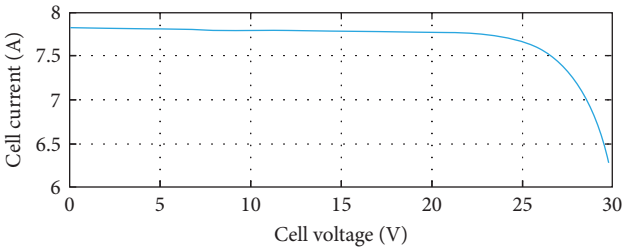

FIGURE 2: I–V characteristics of a single PV cell (25°C/1,000 W/m).

relationship which governs the behavior of the photovoltaic cell is as follows [23]:

$$I = I_{pv} - I_0\left[e^{\frac{q(V+IR_s)}{AKT}} - 1\right] - \frac{V+IR_s}{R_{sh}}, \quad (3)$$

where I is the cell output current (A), V is the cell output voltage (V).

The nonlinearity of the voltage–current properties of photovoltaic modules has made MPP tracking essential. It is extremely important in photovoltaic systems since it reduces the cost of solar panels by minimizing the number of solar modules needed to attain the specified power output. In this document, we use the P&O algorithm (Perturb and Observe algorithm) to generate the PWM reference signals used to control the DC/DC converter, so that the panels operate at their maximum photovoltaic power. The logic of

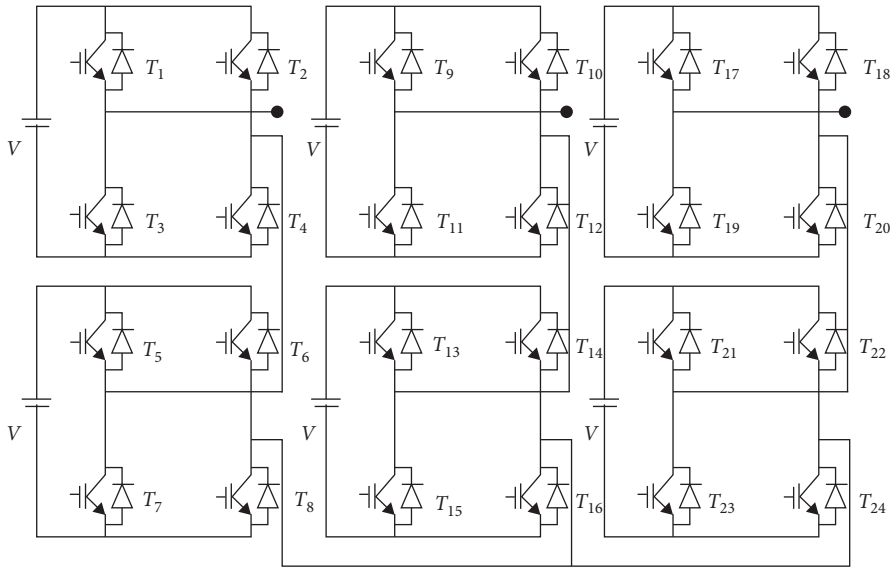

Figure 3: FL-HBCI three-phase voltage inverter.

the P&O algorithm is to perform a perturbation on PV panel voltage while performing the α duty cycle. In fact, after this disturbance, the power provided by the PV panel is calculated in k and compared with the previous power ($k-1$) [24].

2.2. FL-HBCI Topology. Compared to the traditional inverters, the use of MLIs in power circuits has many benefits, such as the reduction of THD, the reduction of stress across static switches, the reduction of power losses and filter volume, and the improvement of power factor with the increase of the voltage level [18]. There are generally three conventional categories of MLIs; the CHBMLI is the most commonly operated in industrial systems because of its high reliability, modularity, high-voltage capability, and power [3]. FLIs offer better performance than three-level and two-level inverters. What is more, they reduce harmonics and cut losses in motor drives [25]. Figure 3 shows a simplified FL-HBCI circuit. Its structure is modular, with each phase comprising two separate DC voltages, resulting in five output voltage levels: +2 V, +V, 0, −V, and −2 V.

(i) +2 V when T_3, T_2, T_7, and T_6 are switched ON.
(ii) +V when T_3, T_2, T_7, and T_8 are switched ON
(iii) 0 when T_3, T_2, T_8, and T_5 are on ON.
(iv) −V when T_3, T_5, T_8, and T_4 are switched ON.
(v) −2 V when T_4, T_5, T_8, and T_1 are turned ON.

In this article, the space vector pulse width modulation (SVPWM) technique for efficiently controlling the five-level inverter is used. This is an advanced control method used in MLIs to generate voltage output signals from a DC source. The main advantage of SVPWM over other control methods lies in its excellent output signal quality and higher efficiency. The technology used in this method consists of decomposing the geometrical vector diagram into hexagonal shapes that represent the lower-level vector diagram of the inverter (Figure 4). In particular, the vector diagram of an FLI can be viewed as composed of six hexagons, each representing a three-level inverter vector diagram. Furthermore, each vector diagram of the three-level inverter can be further divided into six hexagons, each representing the vector diagram of the two-level inverter. This geometric breakdown streamlines the algorithm, transitioning from the modulation of the FLI's vector to that of the two-level inverter's vector, leading to simplification and improved efficiency in the control process. Depending on the desired voltage command, the SVPWM generates an appropriate combination of these vectors to obtain the desired output voltage [9, 12]. An algorithm that handles 125 switching states and 61 switching vectors based on the SVM approach is proposed. This approach eliminates the need for the four carrier signals used in the case of PWM control.

2.3. Model of Induction Motor and IFOC. In a two-phase reference frame (d, q), the magnetizing flow equations of an induction motor are illustrated as follows:

$$\frac{d\Phi_{dr}}{dt} = \frac{L_m}{L_r} R_r i_{ds} - \frac{R_r}{L_r}\Phi_{dr} + (\omega_s - W)\Phi_{qr}, \tag{4}$$

$$\frac{\Phi_{qr}}{dt} = \frac{L_m}{L_r} R_r i_{qs} - \frac{R_r}{L_r}\Phi_{qr} + (W - \omega_s)\Phi_{dr}. \tag{5}$$

Furthermore, in a two-phase operation, the stator currents of the induction motor (V_{ds}, V_{qs}) are defined as follows:

$$\frac{di_{ds}}{dt} = \frac{V_{ds}}{L_s\sigma} - \frac{i_{ds}}{T_s\sigma} - \frac{L_m}{L_r L_s \sigma}\frac{\Phi_r}{dt}, \tag{6}$$

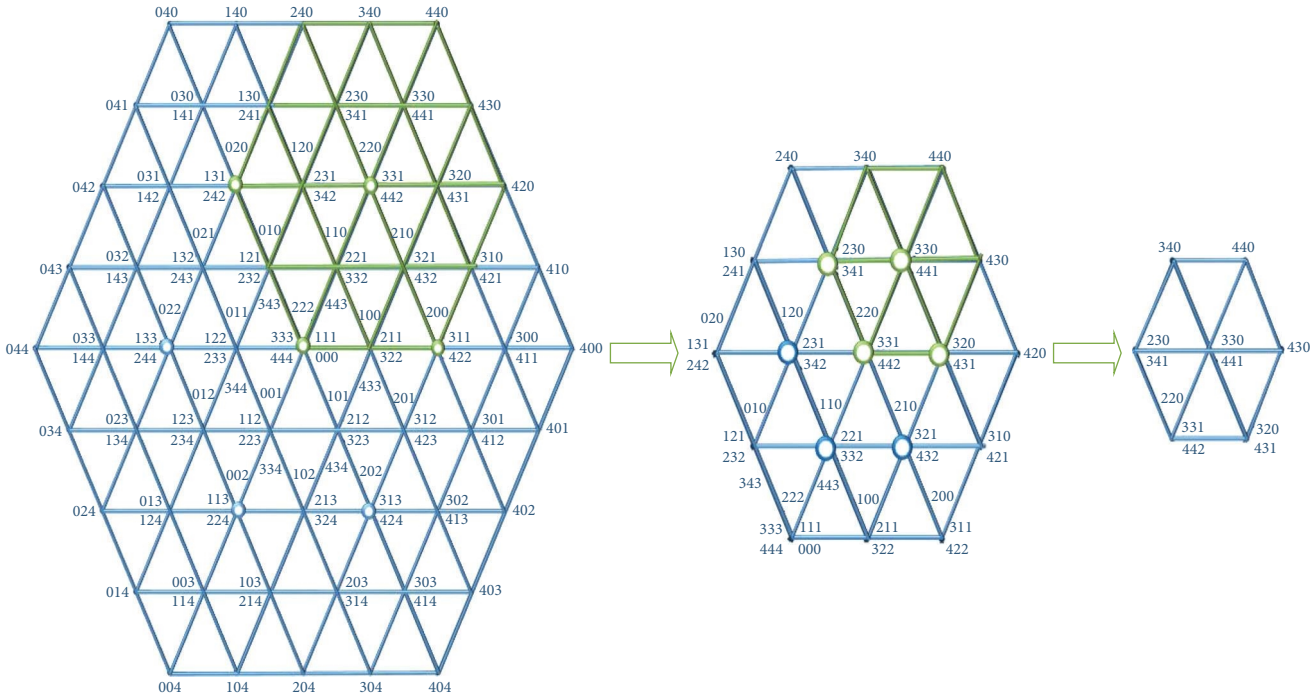

FIGURE 4: Decomposition of the five-level inverter vector diagram.

$$\frac{di_{qs}}{dt} = \frac{V_{qs}}{L_s\sigma} - \frac{i_{qs}}{T_s\sigma} - \frac{L_m\omega_s}{L_rL_s\sigma}\Phi_r, \tag{7}$$

Where

$$T_s = \frac{L_s}{R_s}, \quad \sigma = 1 - \frac{L_m^2}{L_rL_s}. \tag{8}$$

An induction motor's electromagnetic torque (C_{em}) and rotor speed (Ω) on the (d–q) axis are determined as follows:

$$\frac{d\Omega}{dt} = \frac{C_{em}}{j} - \frac{f_r}{j}\Omega - \frac{C_r}{j}, \tag{9}$$

$$C_{em} = p\frac{L_m}{L_r}\left(\Phi_{dr}i_{qs} - \Phi_{qr}i_{ds}\right), \tag{10}$$

where p is the number of poles, L_m is mutual inductance, Φ_r is the rotor flux magnitude, i_{ds}, i_{qs} are stator current of d and q axis, ω_s is the synchronous speed, and C_r is the load torque, j is the moment of inertia.

The fluxes equations, in the context of decoupling control, are expressed in the following form:

$$\Phi_{dr} = \Phi_r = \text{cte}, \tag{11}$$

$$\Phi_{qr} = 0. \tag{12}$$

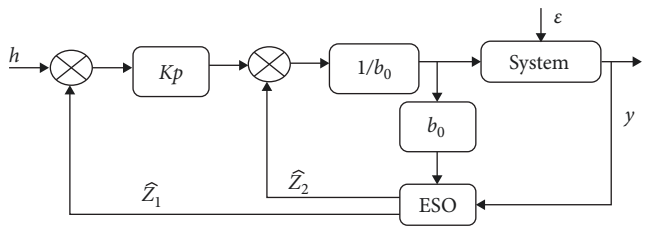

FIGURE 5: ADRC controller.

Equations (5) and (10) become:

$$\Phi_r = L_m i_{ds}, \tag{13}$$

$$C_{em} = p\frac{L_m}{L_r}\Phi_r i_{qs}. \tag{14}$$

3. ADRC

For a sensorless system powered by an FL-HBCI induction motor, various types of internal (resistance variation) and external (load torque, speed variation) disturbances are likely to influence IFOC operation. For this reason, active disturbance rejection control is used as a reliable control method. ADRC is the result of PI derivation, the key to its success. This is a control based on errors rather than on a model [13]. By implementing the extended state observer (ESO), it can evaluate disturbances and uncertainties as an extended state of the system. Figure 5 illustrates the structure of an ADRC.

The system is, in our case, first-order. Moreover, generally, the canonical form of the first-order system is as follows:

$$y = f(y, \varepsilon, t) + b_0 u, \tag{15}$$

where u is an input variable, y is an output variable, b_0 is a constant, and ε is a total of external and internal disturbances.

Using the state-space form, Equation (15) is as follows:

$$\begin{cases} y = \begin{pmatrix} 1 \\ 0 \end{pmatrix}^T .x \\ \dot{x} = \begin{pmatrix} 0 & 1 \\ 0 & 0 \end{pmatrix} .x + \begin{pmatrix} 1 \\ 0 \end{pmatrix} .b_0 u + \begin{pmatrix} 0 \\ 1 \end{pmatrix} .\dot{f} \end{cases}. \tag{16}$$

ESO is given by the following equation:

$$\begin{cases} \widehat{y} = \begin{pmatrix} 1 \\ 0 \end{pmatrix}^T .z \\ \dot{z} = \begin{pmatrix} 0 & 1 \\ 0 & 0 \end{pmatrix} .z + \begin{pmatrix} 1 \\ 0 \end{pmatrix} .b_0 u + \begin{pmatrix} 2\omega_0 \\ \omega_0^2 \end{pmatrix} .(y - \widehat{y}) \end{cases}, \tag{17}$$

with ω_0 the observer bandwidth, determined by pole placement, in order to provide a fast, high-quality output.

According to ADRC, a law of control is then determined by the following:

$$u = \frac{u_0 - z_2}{b_0}, \tag{18}$$

with z_2 being a correct estimation of "f" and z_1 a correct estimation of "y."

The resulting Equation (15) becomes the following:

$$\begin{cases} u_0 = K_p(h - z_1) \\ \dot{y} = u_0 + (f - z_2) \approx u_0 \end{cases}, \tag{19}$$

where h is the reference input signal.

Equations (6), (7), and (9) above can be written in ADRC canonical form as the corresponding equations below:

$$\frac{di_{ds}}{dt} = f_d(i_{ds}, \varepsilon, t) + \frac{V_{ds}(t)}{L_s \sigma}, \tag{20}$$

$$\frac{di_{qs}}{dt} = f_q(i_{qs}, \varepsilon, t) + \frac{V_{qs}(t)}{L_s \sigma}, \tag{21}$$

$$\frac{d\Omega}{dt} = f_\Omega(\Omega, \varepsilon, t) + \frac{C_{em}(t)}{j}. \tag{22}$$

4. Examined Methods

4.1. Luenberger Observer. The first method consists of calculating the angular speed using the Luenberger observer. To obtain the errors, the measured values (stator voltage and currents) are compared with the values estimated using an adaptive model. Once this error has been obtained, the PI controller multiplies it to produce the estimated speed [21].

In this case, the LO is as follows:

$$\begin{cases} \widehat{y} = A.\widehat{x} \\ \dot{\widehat{x}} = B.\widehat{x} + \mathrm{Cu} + D.(y - \widehat{y}) \end{cases}, \tag{23}$$

With

$$A = \begin{bmatrix} -\frac{1}{\sigma}\left(\frac{1}{T_s} + \frac{(1-\sigma)R_r}{L_r}\right) & 0 & \frac{L_m R_r}{\sigma L_s L_r^2} & \frac{L_m W}{\sigma L_s L_r} \\ 0 & -\frac{1}{\sigma}\left(\frac{1}{T_s} + \frac{(1-\sigma)R_r}{L_r}\right) & \frac{L_m W}{\sigma L_s L_r} & \frac{L_m R_r}{\sigma L_s L_r^2} \\ \frac{L_m R_r}{L_r} & 0 & -\frac{R_r}{L_r} & -W \\ 0 & \frac{L_m R_r}{L_r} & W & -\frac{R_r}{L_r} \end{bmatrix}, \tag{24}$$

$$B = \begin{bmatrix} \frac{1}{\sigma L_s} & 0 & 0 & 0 \\ 0 & \frac{1}{\sigma L_s} & 0 & 0 \end{bmatrix}, \tag{25}$$

$$C = \begin{bmatrix} 1 & 0 & 0 & 0 \\ 0 & 1 & 0 & 0 \end{bmatrix}, \tag{26}$$

$$D = \begin{bmatrix} L_{11} & L_{12} & L_{13} & L_{14} \\ -L_{12} & L_{11} & -L_{14} & L_{13} \end{bmatrix}, \tag{27}$$

$$L_{11} = (k-1)\left(\frac{1}{\sigma}\left(\frac{1}{T_s} + \frac{(1-\sigma)R_r}{L_r}\right) + \frac{R_r}{L_r}\right), \tag{28}$$

$$L_{12} = (1-k)W, \tag{29}$$

$$L_{13} = (1-k^2)\left(\frac{L_m R_r}{L_r} - \frac{L_s L_r}{L_m}\left(\frac{1}{T_s} + \frac{(1-\sigma)R_r}{L_r}\right)\right) + \frac{L_s L_r (1-k)}{L_m}\left(\frac{1}{\sigma}\left(\frac{1}{T_s} + \frac{(1-\sigma)R_r}{L_r}\right) + \frac{R_r}{L_r}\right), \tag{30}$$

$$L_{14} = \frac{\sigma L_s L_r W(1-k)}{L_m}. \tag{31}$$

To assure stability, the Lyapunov function is used as follows:

$$V = (x-\widehat{x})(x-\widehat{x})^T + \frac{\left(W-\widehat{W}\right)^2}{\rho}. \tag{32}$$

With ρ being a positive constant coefficient. $x-\widehat{x}$ is the estimation error vector of the induction motor and LO.

The derivative of V in time, which should be negative, is defined by the following equation:

$$\frac{dV}{dt} = \frac{d(x-\widehat{x})}{dt}(x-\widehat{x})^T + \frac{d(x-\widehat{x})^T}{dt}(x-\widehat{x}) + \frac{1}{\rho}\frac{\left(dW-\widehat{W}\right)^2}{dt}. \tag{33}$$

Equation (22) can be developed by the following:

$$\frac{dV}{dt} = [(B-AD)^T + (B-AD)](x-\widehat{x})^T(x-\widehat{x}) + 2\left(W-\widehat{W}\right)\frac{\sigma L_s L_r \widehat{W}(1-k)}{L_m}\left(\widehat{\varphi_{\beta r}}\left(i_{\alpha s}-\widehat{i_{\alpha s}}\right) - \widehat{\varphi_{\alpha r}}\left(i_{\beta s}-\widehat{i_{\beta s}}\right)\right) - \frac{2\left(W-\widehat{W}\right)}{\rho}\frac{d\widehat{W}}{dt}. \tag{34}$$

The expression $[(B-AD)^T + (B-AD)](x-\widehat{x})^T(x-\widehat{x})$ is always negative. Both last terms may be set to zero since they are insignificant in comparison with the first [26, 27].

$$2\left(W-\widehat{W}\right)\frac{\sigma L_r L_s W(1-k)}{L_m}\left(\widehat{\varphi_{\beta r}}\left(i_{\alpha s}-\widehat{i_{\alpha s}}\right) - \widehat{\varphi_{\alpha r}}\left(i_{\beta s}-\widehat{i_{\beta s}}\right)\right) - \frac{2\left(W-\widehat{W}\right)}{\rho}\frac{d\widehat{W}}{dt} = 0. \tag{35}$$

Thus,

$$\widehat{W} = \rho\frac{\sigma L_s L_r W(1-k)}{L_m}\int\left(\widehat{\varphi_{\beta r}}\left(i_{\alpha s}-\widehat{i_{\alpha s}}\right) - \widehat{\varphi_{\alpha r}}\left(i_{\beta s}-\widehat{i_{\beta s}}\right)\right)dt. \tag{36}$$

Many scientists have suggested a PI adaptation mechanism for improving estimation accuracy. It gives the following expression for the estimated speed:

$$\widehat{W} = \left(K_p + \frac{K_i}{s}\right)\left(\widehat{\varphi_{\beta r}}\left(i_{\alpha s}-\widehat{i_{\alpha s}}\right) - \widehat{\varphi_{\alpha r}}\left(i_{\beta s}-\widehat{i_{\beta s}}\right)\right), \tag{37}$$

where K_p and K_i are positive constants.

4.2. Model Reference Adaptive System. MRAS is the second method examined. This method involves calculating two models in parallel. These two models calculate the same variable from different inputs. The induction state variables are obtained from a reduced-order model (model 1), represented by Dybkowski [20]:

$$\frac{d\varphi_{\alpha r}}{dt} = \frac{L_r}{L_m}\left(v_{\alpha s} - R_s i_{\alpha s} - \sigma L_s\frac{di_{\alpha s}}{dt}\right), \tag{38}$$

$$\frac{d\varphi_{\beta r}}{dt} = \frac{L_r}{L_m}\left(v_{\beta s} - R_s i_{\beta s} - \sigma L_s\frac{di_{\beta s}}{dt}\right). \tag{39}$$

In the reference model, these variables are estimated and then compared with the state estimated using the adaptive model. This makes it possible to compare the values estimated from the reference model with those obtained from the subsequent adaptive model (model 2):

$$\frac{d\widehat{\varphi_{\alpha r}}}{dt} = \frac{L_m L_r}{R_r} i_{\alpha s} + \left(\widehat{W} - \frac{L_r}{R_r}\right)\widehat{\varphi_{\alpha r}}, \tag{40}$$

$$\frac{d\widehat{\varphi_{\beta r}}}{dt} = \frac{L_m L_r}{R_r} i_{\beta s} + \left(\widehat{W} - \frac{L_r}{R_r}\right)\widehat{\varphi_{\beta r}}. \tag{41}$$

During motor operation, a difference arises between the outputs of the two models. The dynamic error between the two models is given by the following:

$$e = \varphi_{\alpha r}.\widehat{\varphi_{\beta r}} - \varphi_{\beta r}.\widehat{\varphi_{\alpha r}}. \tag{42}$$

According to the Popov criterion, the estimated speed can be written as the sum of two functions:

$$\widehat{W} = f_1 + \int_0^t f_2 dt. \tag{43}$$

This criterion requires the satisfaction of the following inequality:

$$\int_0^t e.\left(W-\widehat{W}\right)dt \geq -\gamma^2, \tag{44}$$

where γ a positive constant

By replacing the error and the estimated speed with their expressions, Equation (44) becomes the following:

Table 2: Parameters of induction machine.

Symbol	Parameter	Value
L_s	Principal machine inductance	0, 3,973 H
L_r	Seconder machine inductance	0, 3,558 H
R_r	Rotor resistance	5.4 Ω
R_s	Stator resistance	6.8 Ω
L_m	Mutual inductance	0, 39 H
P	Number of pole pairs	2
j	Inertia moment	0.02 kg.m^2
F_v	Viscous friction coefficient	0.0025 N.m.s/rad
P	Power	1 k

$$\int_0^t \left(\varphi_{\alpha r}.\widehat{\varphi_{\beta r}} - \varphi_{\beta r}.\widehat{\varphi_{\alpha r}}\right)\left(W - \left(f_1 + \int_0^t f_2 dt\right)\right)dt > -\gamma^2. \tag{45}$$

To find the two functions f_1 and f_2, we used this mathematical expression:

$$\int_0^t \frac{df}{dt} f dt \geq \frac{1}{2} k_m {f_0}^2. \tag{46}$$

With k_m is a positive constant and f_0 represents the initial condition. The two functions found are as follows:

$$f_1 = K_{p1}\left(\varphi_{\alpha r}.\widehat{\varphi_{\beta r}} - \varphi_{\beta r}.\widehat{\varphi_{\alpha r}}\right), \tag{47}$$

$$f_2 = K_{i1}\left(\varphi_{\alpha r}.\widehat{\varphi_{\beta r}} - \varphi_{\beta r}.\widehat{\varphi_{\alpha r}}\right), \tag{48}$$

where K_{p1} and K_{i1} are positive constants.

According to Equations (42), (47), and (48), the speed becomes the following:

$$\widehat{W} = \left(K_{p1} + \frac{K_{i1}}{s}\right).e. \tag{49}$$

This difference serves as input to the control mechanism, the PI controller in this case, whose work is linked to the adaptive model. The feedback loop forces the control deviation to approach zero. Once the variation reaches zero, the parameter is correctly estimated, and consequently, the speed is properly calculated. The estimated speed value becomes closer to the actual motor speed as the gap becomes smaller.

5. Results of Simulation

Test of the theoretical analysis and design of the system is carried out using MATLAB/Simulink environments. The numerical parameters of the induction motor are provided in Table 2 [1]. To evaluate the performance of the suggested ADRC control for the sensorless IM-fed five-level cascaded inverter, different conditions are applied. Thus, the reference speed value W is maintained at 100 rad/s from 0 to 3 s, then decreases to −100 rad/s from 3 to 8 s and increases to 0 rad/s. In addition, from 1.5 to 5 s, the load torque C_r is applied with a value of 0 N.m, then increases to 5 N.m from 1.5 to 5 s, then decreases to −5 N.m from 5 to 7 s and rises again to 0 N.m. The reference of the flux rotor is maintained at 0.89 Wb. The rotor position is estimated using two different estimators, the MRAS estimator and the Luenberger estimator.

5.1. Speed Variation and Load Torque Variation. In the first section, Figure 6 illustrates the significant impact of selecting the appropriate PV power supply on the input voltages of the machine. To assess the resilience of our system, we subjected it to a variable irradiation ranging from 1,000 W/m^2 to 0.5 s, subsequently increasing to 1,250 W/m^2. It is noteworthy that the ripple does not exceed 1% of the steady-state voltage value, with Dv = 0.01 V being a highly acceptable deviation compared to the continuous voltage, which is approximately 33 V.

Subsequently, Figure 7 presents the outcome of simulating the output voltage achieved at the cascaded converter's output using the SVM approach.

The electromagnetic torque also fluctuates proportionally to the stator currents in i_{sq} quadrature. The ADRC-based control strategy achieves perfect decoupling between the IM's electromagnetic torque and rotor flux. Figures 8 and 9 show that the i_d and i_q currents follow their references perfectly, demonstrating that the parameters are properly chosen.

Figure 10 shows the rotor speed output of the two estimators, which both performed correctly. Therefore, the impact on the mechanical speed depends on the adaptation mechanism used by each observer. Indeed, the observer Luenberger is an observer of the rank 4, and the due of MRAS is based on an observer of reduced order. So, as long as the rank of the observation matrix is high, the speed of filtering is better.

Figure 11 clearly shows the torque performance of two systems. Simulation results show that the IM with an FLI achieves satisfactory sensorless control performance with minimum ripple. The comparison shows that both systems give satisfactory results; torque ripples have been minimized with the use of the MLI.

The curve Figure 12 clearly shows the evolution of the rotor flow component along the axis $O\alpha$. In this figure, we find the evolution of this component of the asynchronous machine obtained from the MRAS estimator and that obtained from the Lunenberg observer. The two curves are identical.

The curve Figure 13 shows the evolution of the rotor flow component along the axis $O\beta$. In this figure, we find the evolution of this component of the induction machine obtained from the MRAS estimator and that obtained from the Lunenberg observer. Similarly, the error between the two components on the $O\beta$ axis converges to 0.

5.2. Robustness Test (Variation of the Resistance and the Moment of Inertia). In the second section, the robustness test consists of varying the rotor resistor Rr, the moment of inertia J, and the stator resistor of the IM. Indeed, the regulators' calculations are based on functions whose

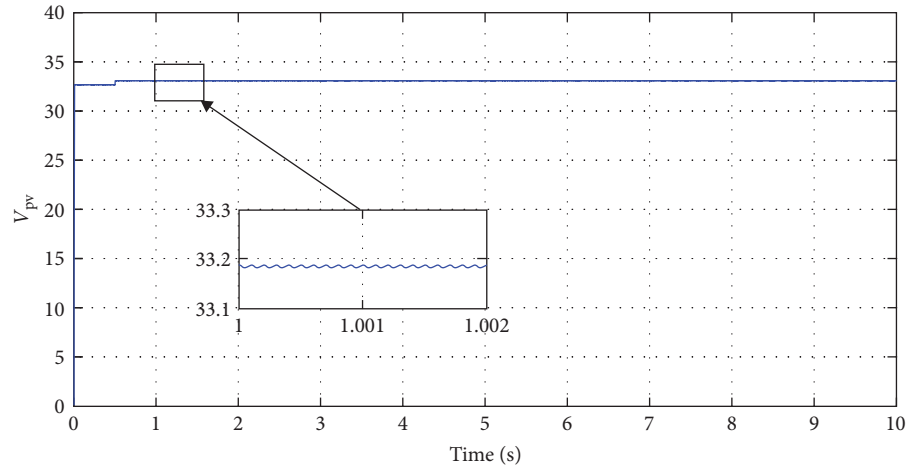

Figure 6: Solar power supply impact on input voltages.

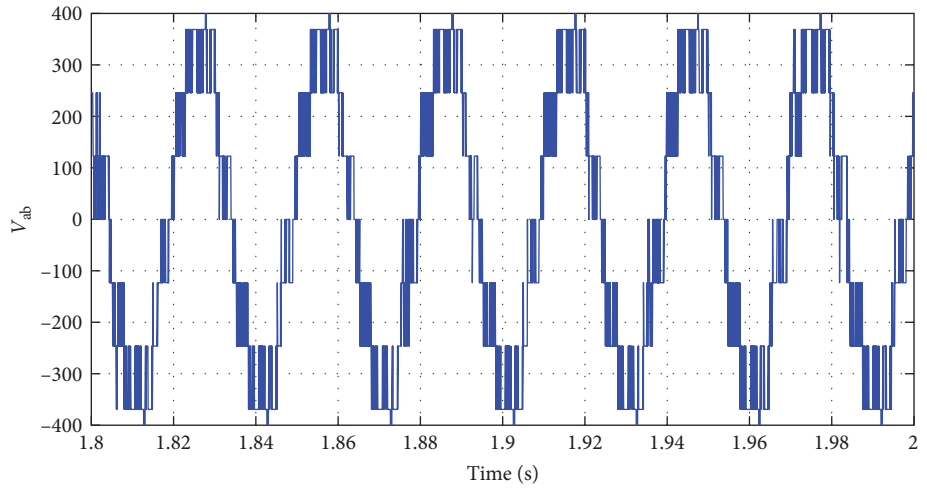

Figure 7: V_{ab} for FL-HBCI on ADR-IFOC.

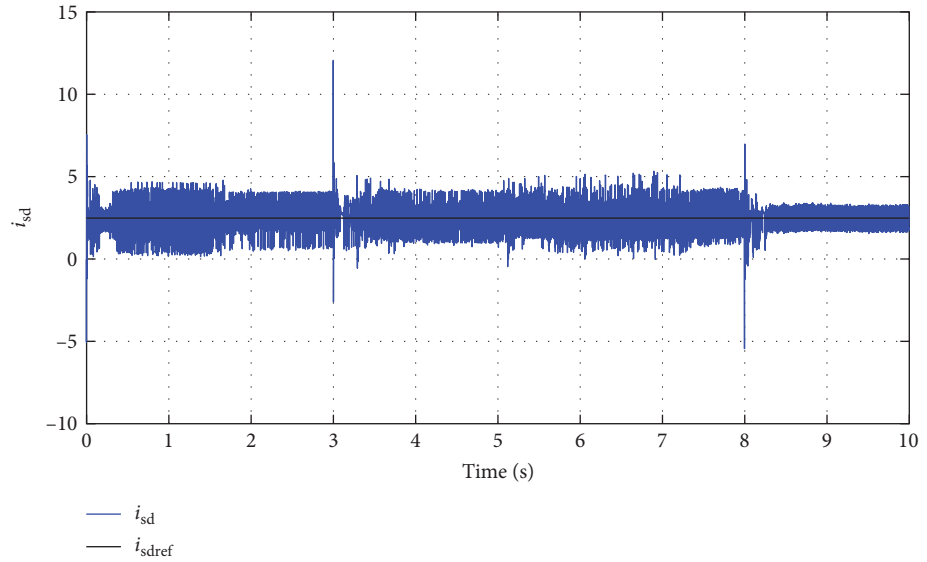

Figure 8: Direct current for ADRC used for IM fed by FL-HBCI.

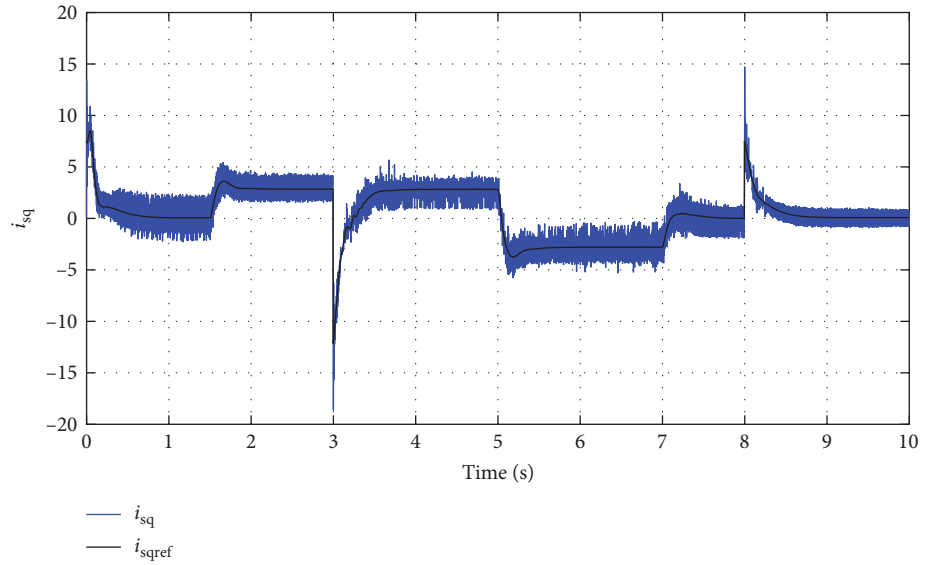

Figure 9: Indirect current for ADRC used for IM fed by FL-HBCI.

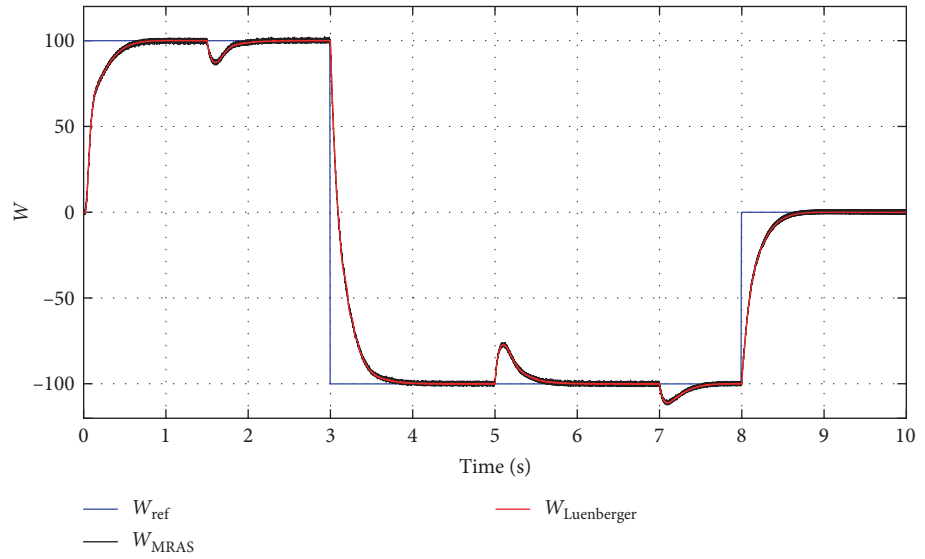

Figure 10: Rotor speed for MRAS and Luenberger for IM fed by FL-HBCI.

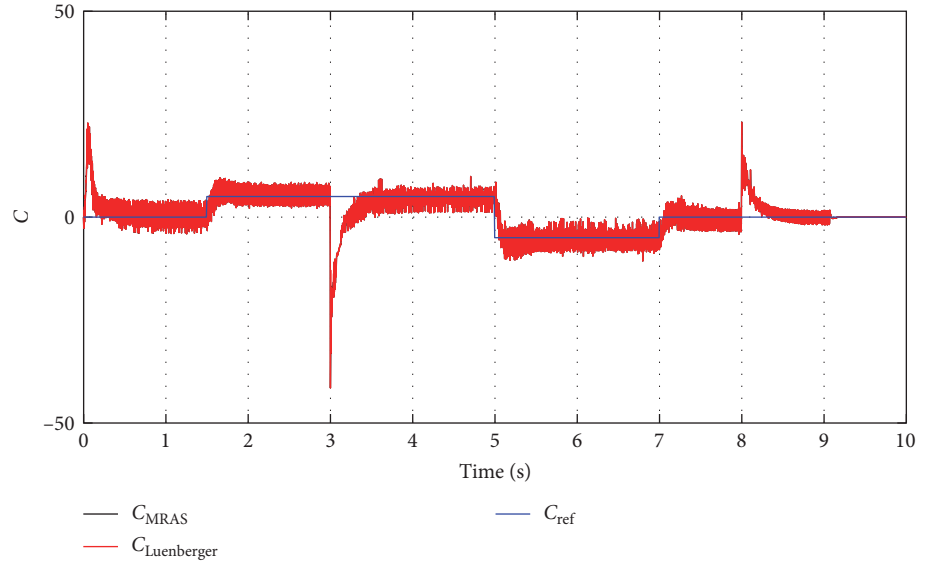

Figure 11: Torque for MRAS and Luenberger for IM fed by FL-HBCI.

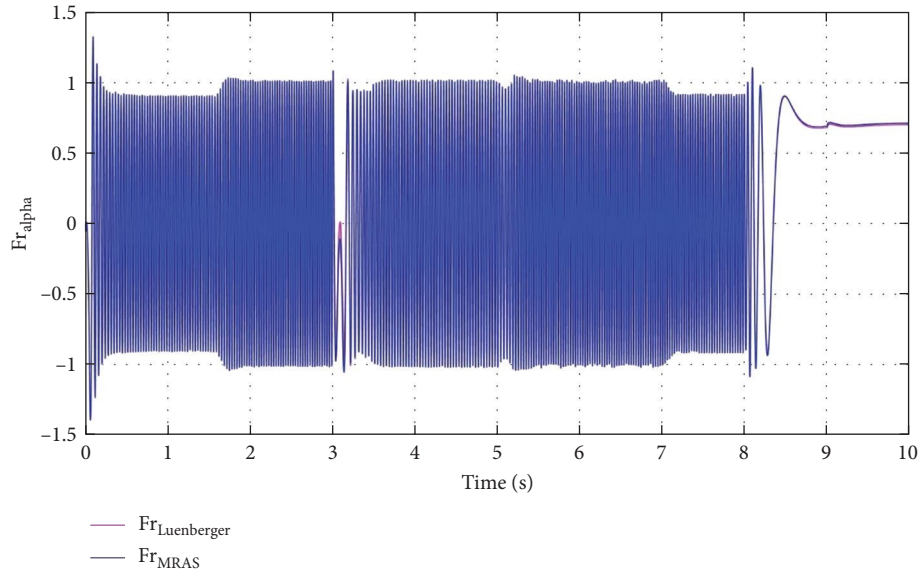

Figure 12: Alpha flow for MRAS and Luenberger.

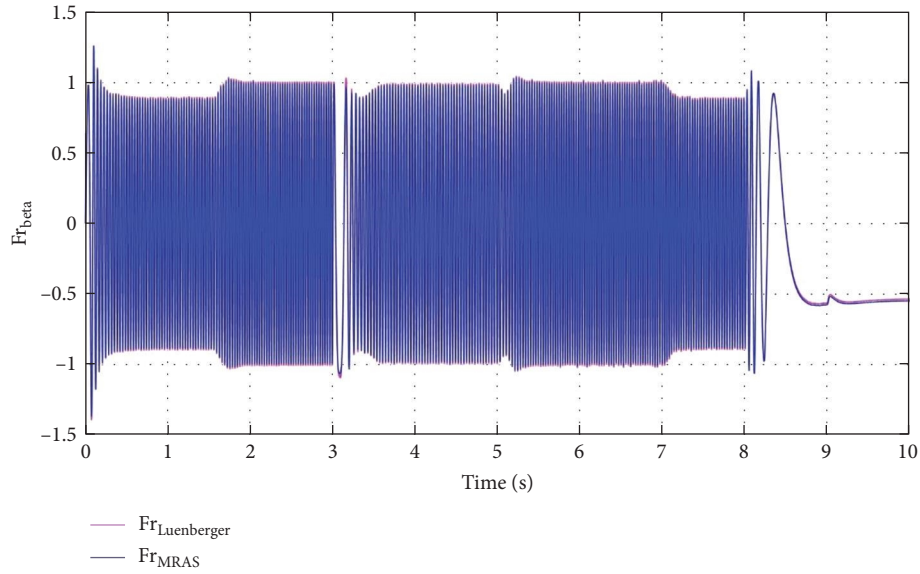

Figure 13: Beta flow for MRAS and Luenberger.

parameters are assumed to be fixed. However, in a real system, these parameters are subject to variations driven by different physical phenomena. Figure 14(a) shows the actual speed and the observed speed from the Luenberger observer, while Figure 14(b) shows the actual speed and the estimated speed from the MRAS estimator. The simulations were performed under a variation of 50% of the value of the rotor resistance Rr, the moment of inertia J, and the stator resistor at a time of 2.5 s. It is noted that (from moment 2.5 s), the static error between the actual and observed speed using the LO observer is much lower than that obtained from the MRAS estimator (Figure 14(c)). This justifies that the MRAS is sensitive to variations in Rs and Rr parameters. Figure 15 shows the evolution of the electromagnetic torque. The variations of these parameters have almost no influence on the machine's operation because the ADRC controllers make it possible to automatically compensate for the disturbances due to these variations. The tracking of the reference is still ensured and the stability of the system is not affected by these parameter variations.

Figure 16 illustrates the rotor speed outputs for both systems, showcasing their successful operation. The graph highlights that, despite torque variations, the ADRC system exhibits a noticeably faster response speed in tracking the reference speed compared to the output speed observed with the PI system. Note that the PI cannot adjust the speed due to variations of several internal and external parameters at the same time.

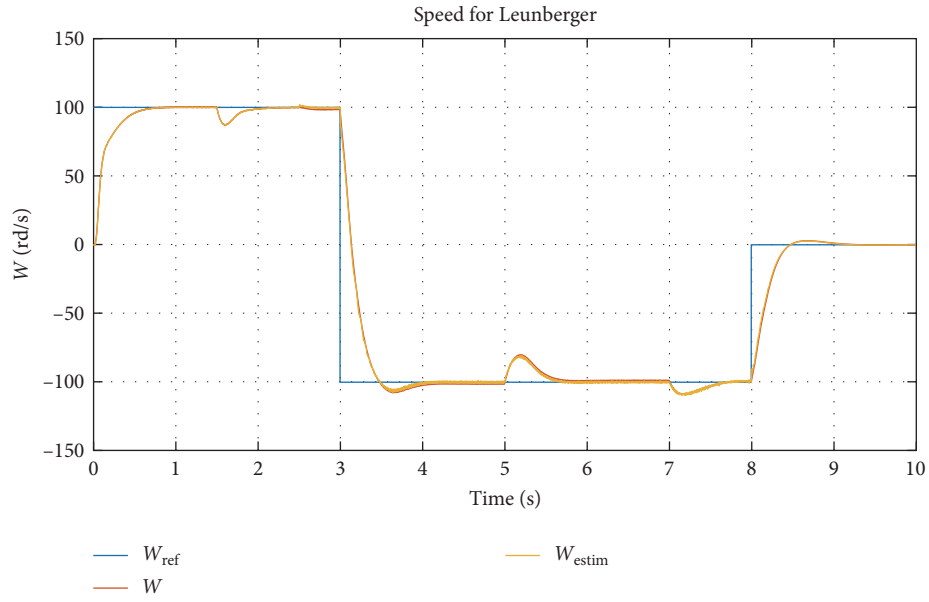

(a)

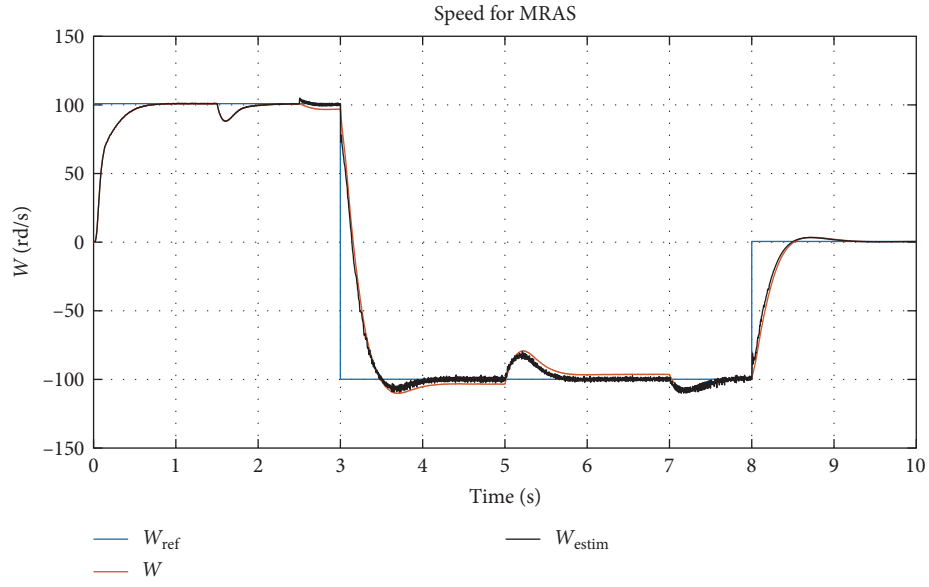

(b)

Figure 14: Continued.

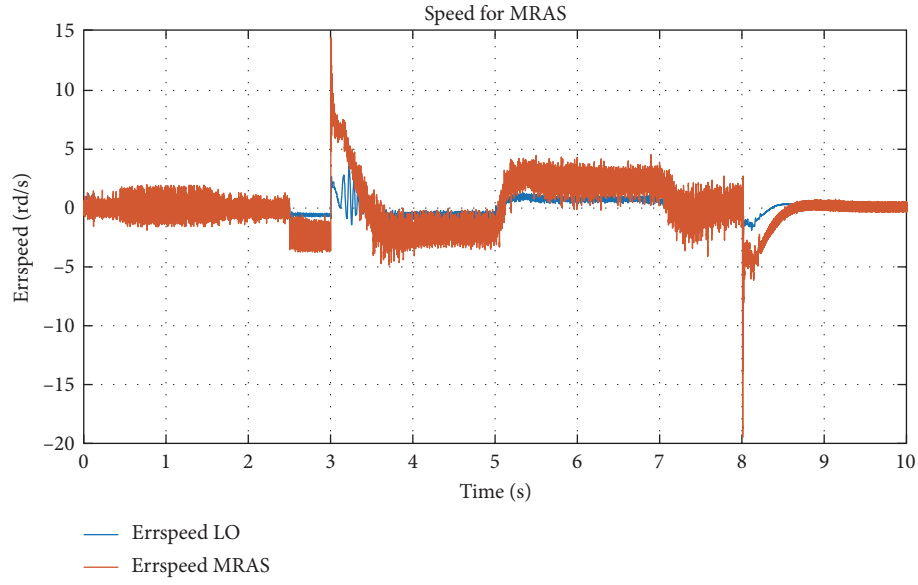

(c)

Figure 14: (a) Rotor speed for Luenberger for IM fed by FL-HBCI, (b) rotor speed for MRAS for IM fed by FL-HBCI, and (c) the error between the actual speed and the estimated speed in both cases (LO and MRAS).

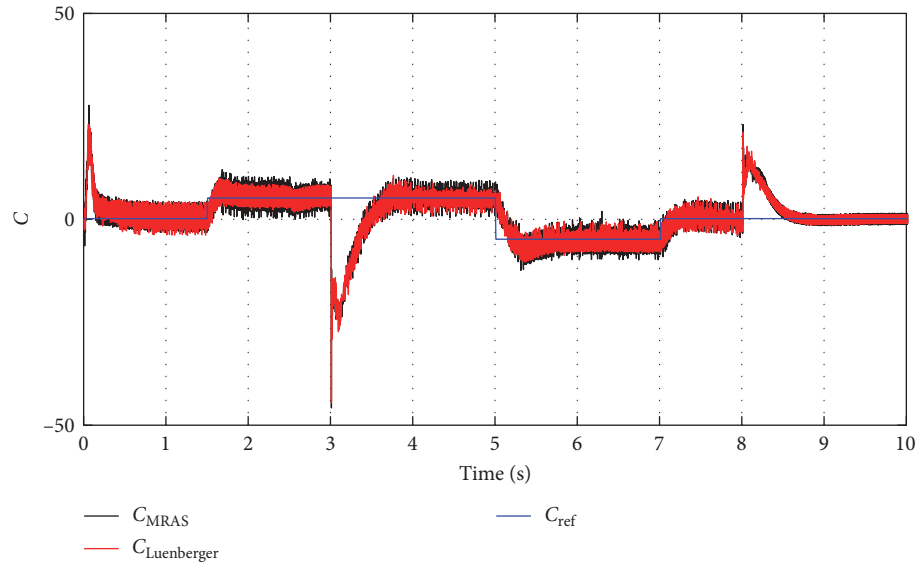

Figure 15: Torque variation for MRAS and Luenberger observers for IM fed by FL-HBCI under resistance and moment of inertia changes.

6. Conclusions

The simulated prototype allows the mechanical speed of an induction machine to be varied without the use of a speed sensor. The combination of the multilevel converter, SVM, ADRC, and Luenberger observer or MRAS has made it possible to reduce signal harmonics and electromagnetic torque ripples. The system was also designed to reject the effects of disturbances. The operating principles and mathematical models of two methods for determining the speed of induction motor drives are analyzed in this article. The results prove that the system with Luenberger is better and more rigid than the MRAS estimator under different scenarios and disturbance conditions. The paper's contribution is a

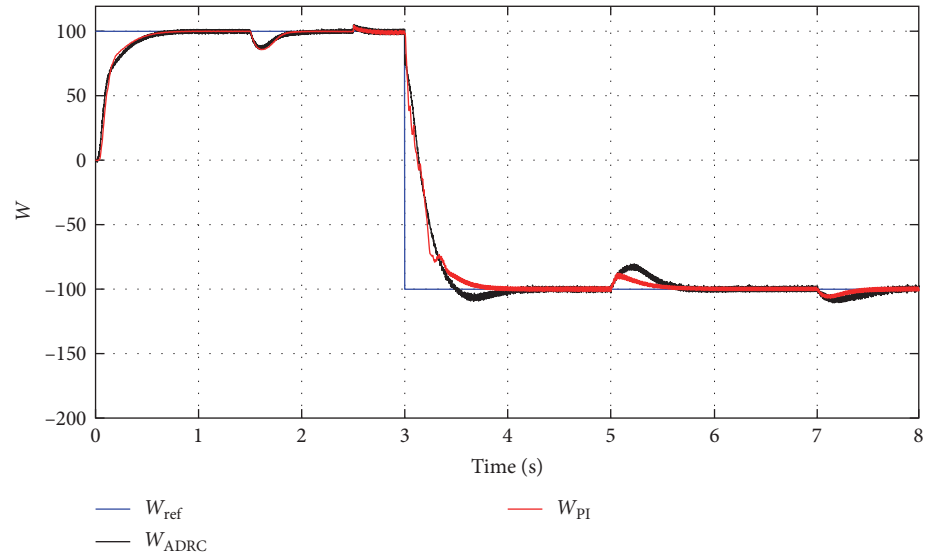

FIGURE 16: Rotor speed for PI and ADRC for IM fed by FL-HBCI.

comparison of the accuracy of the two methods for determining the drive speed of the specific controlled induction motor under the same conditions.

Data Availability

The data used to support the findings of this study are available to all authors upon reasonable request. The data can be made available to the three authors, so request a dataset by sending emails to the addresses of the three authors.

Conflicts of Interest

The authors declare that they have no conflicts of interest.

References

[1] O. Elamri, A. Oukassi, L. El Bahir, and Z. El Idrissi, "Combined vector and direct controls based on five-level inverter for high performance of IM drive," *World Electric Vehicle Journal*, vol. 13, no. 1, Article ID 17, 2022.

[2] C. Li, C. Zhang, J. Liu, and D. Bian, "A high-performance indirect torque control strategy for switched reluctance motor drives," *Mathematical Problems in Engineering*, vol. 2021, Article ID 6618539, 15 pages, 2021.

[3] S. El Bourhichi, A. Oukassi, L. El Bahir, and M. El Adnani, "Active disturbance rejection control for a five-level cascaded H-bridge inverter fed induction motor sensorless field-oriented," *Mathematical Problems in Engineering*, vol. 2021, Article ID 9925072, 13 pages, 2021.

[4] S. Khan, K. Sudhakar, and M. Hazwan bin Yusof, "Techno-environmental analysis of facade integrated photovoltaics and electric vehicle charging for university building," *Mathematical Problems in Engineering*, vol. 2022, Article ID 7186009, 13 pages, 2022.

[5] E. Oumaymah, O. Abdellah, B. Omar, and E. B. Lhoussain, "NPC five level inverter using SVPWM for grid-connected hybrid wind-photovoltaic generation system," *Advances in Science, Technology and Engineering Systems Journal*, vol. 5, no. 6, pp. 981–987, 2020.

[6] S. E. Mountassir, O. Elamri, S. Sarih, A. Tajer, and A. Oukassi, "Instantaneous reactive power control based on five-level inverter for grid connected PV system improvement," *International Review of Electrical Engineering (IREE)*, vol. 17, no. 3, Article ID 286, 2022.

[7] A. Oukassi, S. El Bourhichi, and M. Eladnani, "Indirect vector control of induction motor fed by a five-level cascaded H-bridge inverter using the PV generators," in *2020 International Conference on Electrical and Information Technologies (ICEIT)*, pp. 1–8, IEEE, Rabat, Morocco, March 2020.

[8] A. E. T. Maamar, M. Helaimi, R. Taleb, and A. Gadoum, "Modeling and control of 41-level inverter using best switching angles calculation method," *International Journal of Applied Power Engineering*, vol. 9, no. 2, pp. 153–158, 2020.

[9] E. Oumaymah, O. Abdellah, and E. A. Mustapha, "The injection of wind power into a grid using a multi-level inverter controlled by SVPWM," in *2020 International Conference on Electrical and Information Technologies (ICEIT)*, pp. 1–6, IEEE, Rabat, Morocco, March 2020.

[10] N. X. Doan and N. V. Nguyen, "Virtual space vector pulse width modulation for asymmetric *T*-type neutral point clamped 3-level inverter," *Mathematical Problems in Engineering*, vol. 2021, Article ID 1379040, 19 pages, 2021.

[11] X. Ge, M. Chen, M. Shi et al., "Corrigendum to "a single-stage buck-boost three-level neutral-point-clamped inverter with two input sources for the grid-tied photovoltaic power generation"," *Mathematical Problems in Engineering*, vol. 2019, Article ID 4878134, 1 pages, 2019.

[12] E. Oumaymah, O. Abdellah, B. Omar, and E. B. Lhoussain, "Backstepping design control applied to the wind PMSG generator and grid connection using a multilevel inverter," in *2021 8th International Conference on Electrical and Electronics Engineering (ICEEE)*, pp. 136–141, IEEE, Antalya, Turkey, April 2021.

[13] J. Han, "From PID to active disturbance rejection control," *IEEE Transactions on Industrial Electronics*, vol. 56, no. 3, pp. 900–906, 2009.

[14] A. Oumar, R. Chakib, and M. Cherkaoui, "Modeling and control of double star induction machine by active disturbance rejection control," *TELKOMNIKA (Telecommunication Computing Electronics and Control)*, vol. 18, no. 5, Article ID 2718, 2020.

[15] Z. Chu, "Active disturbance rejection control: applications, stability analysis, and tuning method," 2018, Consulté le: 25 janvier 2024. [En ligne]. Disponible sur: http://hdl.handle.net/1993/33072.

[16] S.-J. Wu, H.-H. Chiang, J.-W. Perng, C.-J. Chen, B.-F. Wu, and T.-T. Lee, "The heterogeneous systems integration design and implementation for lane keeping on a vehicle," *IEEE Transactions on Intelligent Transportation Systems*, vol. 9, no. 2, pp. 246–263, 2008.

[17] M. A. Mossa, N. Vu Quynh, H. Echeikh, and T. D. Do, "Deadbeat-based model predictive voltage control for a sensorless five-phase induction motor drive," *Mathematical Problems in Engineering*, vol. 2020, Article ID 4164526, 30 pages, 2020.

[18] O. Elamri, A. Oukassi, A. E. T. Maamar, and L. El Bahir, "Design and simulation of a power system composed of grid-tied five-level inverter with LCL filter," *Electronics Journal*, vol. 26, no. 1, pp. 17–25, 2022.

[19] K. Pavel and L. Jiří, "Comparison of sensorless AC drive operation using MRAS method or Luenberger observer," in *2017 International Conference on Optimization of Electrical and Electronic Equipment (OPTIM) & 2017 Intl Aegean Conference on Electrical Machines and Power Electronics (ACEMP)*, pp. 281–286, IEEE, Brasov, Romania, May 2017.

[20] M. Dybkowski, "Induction motor stator faults identification using modified MRAS type estimator," *PRZEGLĄD ELEKTROTECHNICZNY*, vol. 1, no. 5, pp. 216–221, 2023.

[21] J. You, W. Wu, and Y. Wang, "An adaptive Luenberger observer for speed-sensorless estimation of induction machines," in *2018 Annual American Control Conference (ACC)*, pp. 307–312, IEEE, Milwaukee, WI, USA, June 2018.

[22] T. Abdelkrim, E. Berkouk, K. Benamrane, and T. Benslimane, "Study and control of 5-level PWM rectifier-5-level NPC active power filter cascade using feedback control and redundant vectors," *Turkish Journal of Electrical Engineering and Computer Sciences*, vol. 20, no. 5, pp. 655–677, 2012.

[23] A. K. Maurya, K. Chahar, and Y. K. Chauhan, "Analysis on photovoltaic assisted three phase five level unipolar PWM inverter for induction motor driven water pumping system," *International Journal of Advanced Computer Research*, vol. 3, no. 1, 2013.

[24] K. Cherifi, Y. Miloud, and M. Mostefai, "A modified multilevel inverter topology with maximum power point tracking for photovoltaic systems," *Journal of Engineering Science and Technology*, vol. 14, no. 1, pp. 351–369, 2019.

[25] G. Li, Y. Wang, and Z. Fu, "Modified multiverse optimizer selective harmonic elimination for five-level modified packed U-cells inverter and analysis of motor torque ripple suppression," *Mathematical Problems in Engineering*, vol. 2022, Article ID 8397836, 12 pages, 2022.

[26] P. Ramasamy and V. Krishnasamy, "SVPWM control strategy for a three phase five level dual inverter fed open-end winding induction motor," *ISA Transactions*, vol. 102, pp. 105–116, 2020.

[27] Y. Huang and W. Xue, "Active disturbance rejection control: methodology and theoretical analysis," *ISA Transactions*, vol. 53, no. 4, pp. 963–976, 2014.